Journal of Materials Chemistry A

PAPER

View Article Online
View Journal | View Issue

Cite this: J. Mater. Chem. A, 2018, 6, 22870

Sandwiched porous C/ZnO/porous C nanosheet battery anodes with a stable solid-electrolyte interphase for fast and long cycling†

Yuting Zhao,[a] Gaoshan Huang,*[a] Dingrun Wang,[a] Yan Ma,[a] Zhongyong Fan,[a] Zhihao Bao[b] and Yongfeng Mei*[a]

Producing carbon/transition metal oxide composites is a promising strategy for improving the stability of high energy alkali-ion batteries. However, fracture of the thin carbon layer by enormous volume change of the oxide and sluggish ion transport in the composite lead to premature cell failure. In this study, we show that anodes consisting of an active ZnO nanosheet sandwiched between two layers of porous thick carbon coating can cycle over 1650 times without obvious capacity decay. The outer thick carbon coating with mechanical robustness suppresses the expansion of the inner oxides without cracks, resulting in a stable SEI layer. Its porous structure and conductive nature also facilitate Li^+/electron transportation into the inner oxides. The battery containing composite nanosheets shows a fast and high capacity of 330 mA h g^{-1} at 5000 mA g^{-1}. We notice that a critical thickness ratio of ZnO to the carbon layer may exist, and the carbon layer is prone to fracture in the case of large thickness ratio. The results have important applications in designing carbon/metal oxide composites for high performance anodes of Li-ion batteries.

Received 13th August 2018
Accepted 15th October 2018

DOI: 10.1039/c8ta07848c

rsc.li/materials-a

Introduction

Transition metal oxides have emerged as the most promising candidate anode for high energy density electrodes due to their high theoretical capacity.[1,2] Recently, the exponentially increased research studies on two-dimensional (2D) metal oxides have offered an unprecedented opportunity for their use in high rate capacity lithium ion batteries.[3–5] The well-designed 2D nanostructures have demonstrated their superiority for fast and long-lifespan lithium storage by providing a shortened ion-diffusion length and releasing the volume change strain.[3–5] However, the destruction of the desirable morphologies of 2D metal oxides could not be truly avoided during repeated expansion and contraction of the lattice.[6] Lithiation induced nanocracks have been observed, and the exposure of fresh oxide to the electrolyte causes further growth of the solid-electrolyte interphase (SEI). The SEI becomes thicker with each charge/discharge cycle and eventually leads to severe capacity decay because of the consumption of electrolyte/Li^+ and its electrically insulating nature.[7–10] Thus it is critical to get a stable SEI for long life anodes made from materials with large volume changes.

To overcome these obstacles, carbonaceous materials are introduced as matrices or surface coating layers to constrain the volume change and control the growth of the SEI layer.[11–15] Among them, sandwich-like hybrid nanosheets in the form of carbon/oxides/carbon, with a conductive carbon coating on both sides of oxides, have manifested a significant improvement in both rate capacity and cycling stability.[10,16–20] Compared with a sandwiched structure with oxides standing on the surfaces of the carbon layer (oxide/carbon/oxide), the carbon coating as the outer surface helps to constrain the volume change and prevents the oxides from reacting with the electrolyte, thus enabling an enhanced lifespan.[16–19] For example, a capacity decay of 70% was observed for the G@SnO_2 composite because of the agglomeration and pulverization of SnO_2 during cycling. After the structure was coated with a uniform carbon layer, the G@SnO_2@C composite demonstrated a much improved cycling stability.[17]

However, a thin layer of surface carbon coating is prone to fracture since excessive stress is developed in the carbon coating during cycling by inner oxide expansion.[21,22] Such fracture of the carbon coating, upon lithiation, would immediately propagate into the oxide core due to the elevated driving force caused by the material inhomogeneity between the coating and the core.[22] The exposed fresh core material reacts with the electrolyte and causes further growth of the SEI. Thus a capacity decay of 25% in 60 cycles was observed in graphene-confined Sn

[a]Department of Materials Science, Fudan University, Shanghai 200433, P. R. China. E-mail: gshuang@fudan.edu.cn; yfm@fudan.edu.cn

[b]Shanghai Key Laboratory of Special Artificial Microstructure Materials and Technology, School of Physical Science and Engineering, Tongji University, Shanghai 200092, P. R. China

† Electronic supplementary information (ESI) available. See DOI: 10.1039/c8ta07848c

nanomembranes with a graphene thickness of 5 nm.[23] Previous investigation demonstrates that the fracture of the carbon layer is closely related to the coating thickness and the thicker one can sustain larger stress.[22] Thus, in order to prevent the fracture of the surface coating layer, a thicker coating for constraining the deformation of inner oxides is desired.[24,25] Nevertheless, a too thick carbon coating would act as a barrier for Li^+ transporting into inner oxides. Moreover, the isolated 2D nanosheets are inclined to restack into a close packed structure. This process would sharply decrease the active surface and block ion transport kinetics.[26,27] In this regard, porous 2D nanostructures, ensuring efficient penetration of the electrolyte and fast charge transfer, are highly desired for improving the power density of batteries.[11,13,28]

In the present work, we therefore designed porous carbon confined oxide nanosheets, in which an oxide layer with controllable thickness was sandwiched between two porous carbon layers with relatively larger thickness (>30 nm). In the methodology, template-assisted atomic layer deposition (ALD) was used to deposit the oxide layer on a self-made organic template, followed by a simple pyrolysis process. The architecture is designed with several superiorities. First, the thick carbon coating on the surface of oxides is thought to constrain the volume expansion of oxides by its mechanical robustness, thus providing a stable SEI.[11,29] Second, the porous feature of the thick carbon coating alleviates the restacking issues of the nanosheets and facilitates Li^+ diffusion into the inner oxides.[26] Third, the carbon outside also provides an electric contact network around oxides. Due to its high theoretical capacity of 978 mA h g^{-1} and natural abundance, ZnO is chosen as the active anode material in the present study. The composite nanosheets (porous carbon/ZnO/porous carbon nanosheets, hereafter CZC nanosheets) in this study maintain high rate capacity and stability. A capacity of 330 mA h g^{-1} was obtained at 5000 mA g^{-1} and no obvious capacity decay was observed after more than 1650 cycles. An optimized thickness ratio between ZnO and the carbon coating ($\sim$1 : 1) was also revealed. In addition, carbon confined TiO_2 composite nanosheets (porous carbon/TiO_2/porous carbon nanosheets, hereafter CTC nanosheets) were fabricated to prove the universality of the current approach. The results obtained here may have important applications in the field of high energy and stable lithium storage.

Experimental section

Preparation of samples

Preparation of a porous organic template. A degradable polyurethane foam template was prepared by crosslinking poly(propylene oxide) (PPO) and poly-(propylene oxide)-*block*-polylactide (PPO-*b*-PLA) copolymers using isocyanate.[30] More details can be found in ESI S1.†

Preparation of CZC nanosheets. The CZC nanosheets were prepared by a template-assisted ALD approach[31,32] and a subsequent pyrolysis process as outlined in Fig. 1a. First, deposition of a ZnO nanomembrane onto a porous organic template was conducted in a home-made reactor at 150 °C. Diethylzinc (DEZ) and deionized water (DIW) were used as precursors. Nitrogen (N_2) gas served as both the carrier and purge gas with a flow rate of 20 sccm. A typical ALD sequence included the following: DEZ pulse (30 ms), waiting time (2 s), N_2 purge (20 ms), DIW pulse (20 ms), waiting time (2 s), and N_2 purge (20 ms). The thickness of the ZnO nanomembrane was controlled by altering the number of ALD cycles (*e.g.*, 50, 100, 200, 400 and 800 cycles in the present work). After the ALD process, the samples were pyrolyzed at 700 °C for 1 h in a N_2 flow of 600 mL min^{-1} to carbonize the organic template. A freestanding interconnected structure was formed, and after being crashed, a large amount of CZC nanosheets were obtained. The nanosheets obtained were washed with ethanol and DIW to remove the residual impurities.

Preparation of CTC nanosheets. The CTC nanosheets were also fabricated by the same strategy. First, TiO_2 was deposited onto the template at 150 °C. Tetrakis(dimethylamido)titanium (TDMAT) and DIW were used as precursors. A typical ALD sequence includes the following: TDMAT pulse (200 ms), waiting time (2 s), N_2 purge (30 s), H_2O pulse (50 ms), waiting time (2 s), and N_2 purge (30 s). After 200 deposition cycles, the sample was pyrolyzed at 700 °C in N_2 flow (600 mL min^{-1}) for 1 h. The nanosheets obtained were washed with ethanol and DIW to remove the residual impurities.

Preparation of ZnO nanosheets. After deposition of ZnO onto the template, the sample was treated in an O_2 atmosphere (600 mL min^{-1}) at 700 °C for 3 h to remove the organic template. The ZnO nanosheets obtained were washed with ethanol and DIW to remove the residual impurities.

Microstructural characterization

The morphologies of the samples were investigated using a scanning electron microscope (SEM, Phenom Prox) and a transmission electron microscope (TEM, Nova NanoSem 450). The energy dispersive spectrum (EDS, Oxford X-Max 80T) was utilized to analyze the composition of the sample. Dual beam focused ion beam (FIB, Helios NanoLab 600) was used to cut the nanosheet for cross-sectional imaging. The crystallinity of the samples was characterized by X-ray diffraction (XRD) on a Bruker D8 X-ray diffractometer with Cu Kα radiation (λ = 1.5418 Å). The X-ray photoemission spectroscopy (XPS) measurements were conducted with a ULVAC PHI5000 VERSA PROBE system. Thermogravimetric analysis (TGA) was performed using an SDT Q600 in the range of 25–900 °C (heating rate: 10 °C min^{-1}) under air-flow. Nitrogen sorption isotherms were measured on a Quadrasorb evo (America Quantachrome). Before measurements, the samples were degassed in a vacuum at 250 °C for 3 h. The Raman spectrum was collected by using a Jobin Yvon LabRAM HR800 spectrometer, excited by a 632.8 nm He–Ne laser with a laser spot size of $\sim$1μm^2.

Electrochemical measurements

The electrochemical tests were performed on a coin-type 2016 half-cell with metallic lithium serving as both the counter and reference electrodes. The working electrode was composed of 80 wt% active material, 10 wt% Super-P (conductive additive agent), and 10 wt% polyvinylidene difluoride (binder). The electrolyte used for Li-ion half cells consisted of 1 M $LiPF_6$

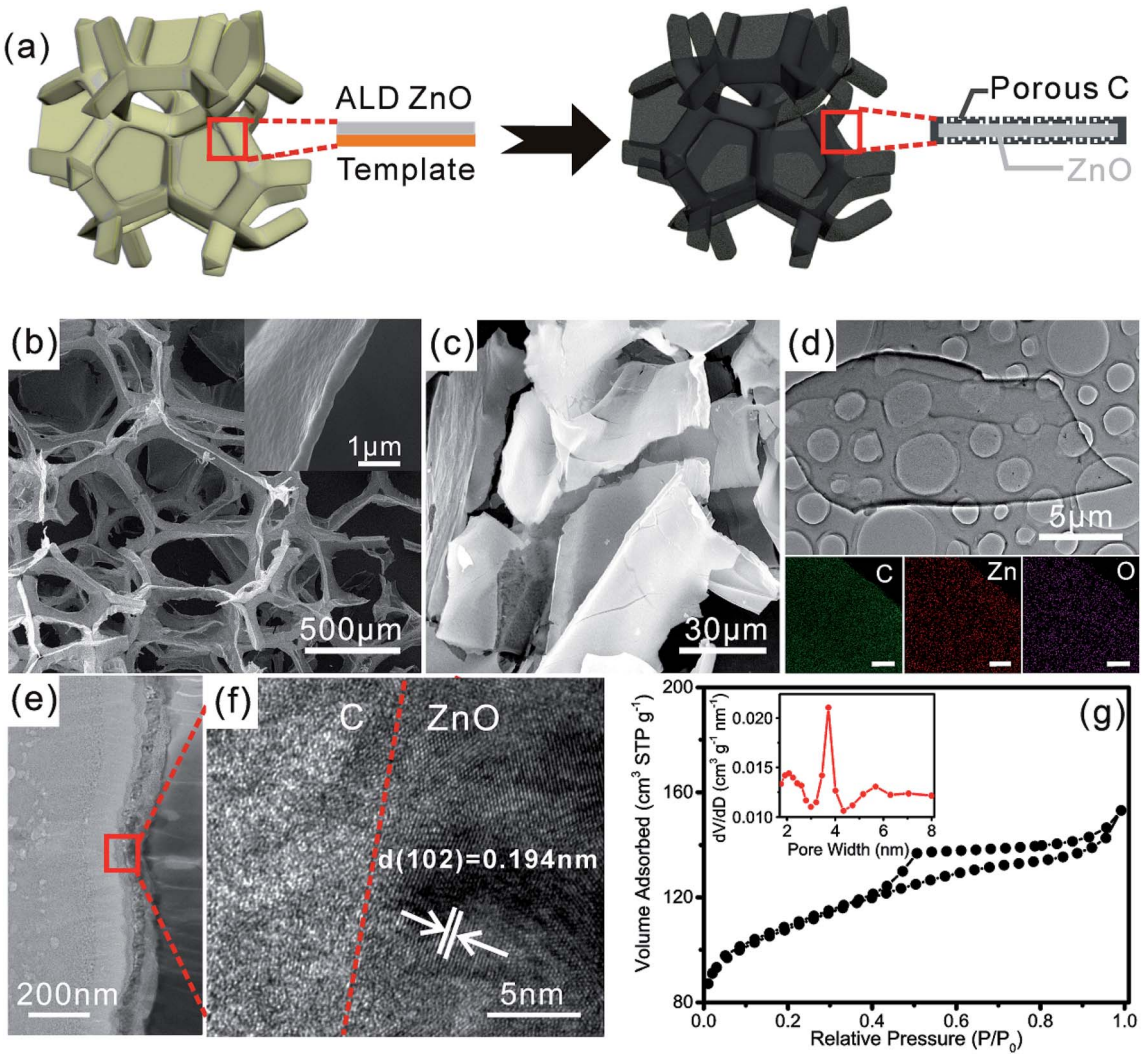

Fig. 1 (a) Schematic of the synthesis procedure of CZC nanosheets. (b) SEM image of the porous network of the sample after pyrolysis. The inset shows a curled edge of a nanosheet. (c) SEM image of CZC nanosheets after being crashed. (d) TEM image and EDS mapping of an individual CZC nanosheet. (e) Cross-sectional TEM image of a CZC nanosheet. The nanosheet is composed of a sandwiched structure. (f) High resolution TEM image of the C/ZnO interface. (g) Nitrogen adsorption–desorption isotherms and pore size distribution (inset) of the CZC nanosheet sample.

solution in a 1 : 1 mixture of ethylene carbonate (EC)/diethyl carbonate (DEC) (Shenzhen Kejing Star Technology CO., LTD). The two electrodes were assembled into a cell in an argon circulating glovebox (H_2O and O_2 <1 ppm). Galvanostatic charge/discharge cycling was carried out on a battery testing system (LAND CT2001A) with a voltage window of 0.001–3 V *vs.* Li^+/Li at different current rates. Electrochemical impedance spectroscopy (EIS) measurements were carried out on a Zennium/IM6 electrochemical workstation in a frequency range from 1 MHz to 100 mHz with an amplitude of 5 mV. CV tests were also carried out at a scan rate of 0.2 mV s^{-1} from 0 to 3 V on a Zennium/IM6 electrochemical workstation.

Results and discussion

The CZC nanosheets were prepared by a template-assisted ALD method[31,32] and a subsequent pyrolysis process as outlined in Fig. 1. The ZnO nanomembrane is first deposited onto the surface of the porous organic template (see Fig. 1a and S2†) and then the ZnO coated template is treated in an inert atmosphere at high temperature. During the pyrolysis process, the template is transferred to carbon.[33,34] Meanwhile, hydrocarbons (*e.g.*, methane, ethane, ethylene, and propylene) are generated with increasing temperature.[35] These volatile products undergo a secondary pyrolytic deposition on all exposed surfaces.[36] After the pyrolysis procedure, a monolith of porous network, with the framework similar to that of the original template, is obtained. Fig. 1b demonstrates the typical morphology of the sample with 200 ALD cycles. The structure consists of interconnected nanosheets, and the inset of Fig. 1b shows a curled edge of a nanosheet, indicating the flexibility. After the porous structure is crashed manually, large amounts of composite nanosheets (*i.e.*, CZC nanosheets) are obtained (Fig. 1c). For a more detailed identification of the structural features and chemical compositions, the EDS of an individual CZC nanosheet was conducted, as shown in Fig. 1d. The corresponding mapping results

indicate the homogeneous distribution of C, Zn, and O elements in the nanosheet. And the atomic concentrations of C, Zn, and O are 47%, 15%, and 38%, respectively. Besides, the cross-sectional structure of the nanosheet was investigated with the help of the FIB technique. From the cross-sectional TEM image (Fig. 1e), one can see that the nanosheet is composed of a three-layer structure with 32 nm-thick ZnO sandwiched between two carbon layers with thicknesses of 30 and 38 nm, respectively. No voids and impurities are observed between the adjacent layers, suggesting a good electrical contact (Fig. 1e and f). The high resolution TEM image in Fig. 1f demonstrates the amorphous structure of the carbon layer and the nanocrystalline feature of ZnO. We notice that enlarged TEM images reveal that a large amount of voids/pores exist in the carbon layer (Fig. S3†). On the basis of the Barrett–Joyner–Halenda model, well-defined average pore sizes of 2.2, 3.8, and 5.8 nm are determined (inset of Fig. 1g). This porous carbon layer, together with the 2D nanosheet geometry, leads to a remarkably enhanced surface area (266 $m^2\ g^{-1}$, see Fig. 1g). This unique structural property is of benefit to fast diffusion of Li^+ in the composite CZC nanosheets and will be discussed later.

The crystallographic structure of the CZC nanosheets was analyzed by XRD. As shown in Fig. S4,† the XRD patterns prove the coexistence of the amorphous carbon layer and multi-crystal ZnO layer after being treated at 700 °C in a N_2 atmosphere. Both CZC nanosheets and ZnO nanosheets show diffraction peaks at $2\theta = 31.769°$, 34.421°, 36.252°, 47.538°, 56.602°, and 62.862°, which are associated with the (100), (002), (101), (102), (110), and (103) lattice planes of hexagonal ZnO (PDF #36-1451), respectively.[37] The Raman spectrum also indicates the amorphous nature of the carbon layer as a very intense D band (1339 cm^{-1}, associated with disordered carbon) is observed (Fig. S5†).[30,32] The chemical bonding states of CZC nanosheets were also studied by XPS measurements (Fig. S6†). The presence of C, O, and Zn elements is confirmed using the characteristic spectra of C 1s, O 1s, and Zn 2p (see the detailed discussion in the ESI†).

Fig. 2a shows the first three cyclic voltammetry (CV) curves of the anode made from CZC nanosheets with 200 ZnO ALD cycles (CZ200C nanosheets, 68% ZnO; Fig. S7†). In the first cathodic scan, four peaks at 1.7, 0.9, and 0.6 and near 0.1 V can be discerned carefully. The peak at 1.7 V is ascribed to the decomposition of the electrolyte to generate a SEI layer and gradually decreases in the subsequent cycles.[38,39] The peak at 0.9 V presumably originates from the conversion reaction between ZnO and Li^+ to form Zn and Li_2O.[38,40] The peak at 0.6 V is ascribed to the multi-step alloying process between Zn and Li^+ to generate Li_xZn. The sharp peak near 0.1 V can be attributed to the insertion of Li^+ into the amorphous carbon.[41] In the subsequent cathodic scans, a broad peak gradually stabilizes at 0.8 V, corresponding to the reduction of ZnO and the alloying process between Zn and Li^+.[42] For the anodic curve, four peaks at 0.2, 0.5, 1.7, and 2.2 V are observed. The oxidation peaks at 0.2 and 0.5 V indicate the multi-step dealloying process of the Li_xZn alloy to form Zn, and the peaks at 1.7 and 2.2 V indicate the oxidation of Zn to generate ZnO.[40,41] It is notable that

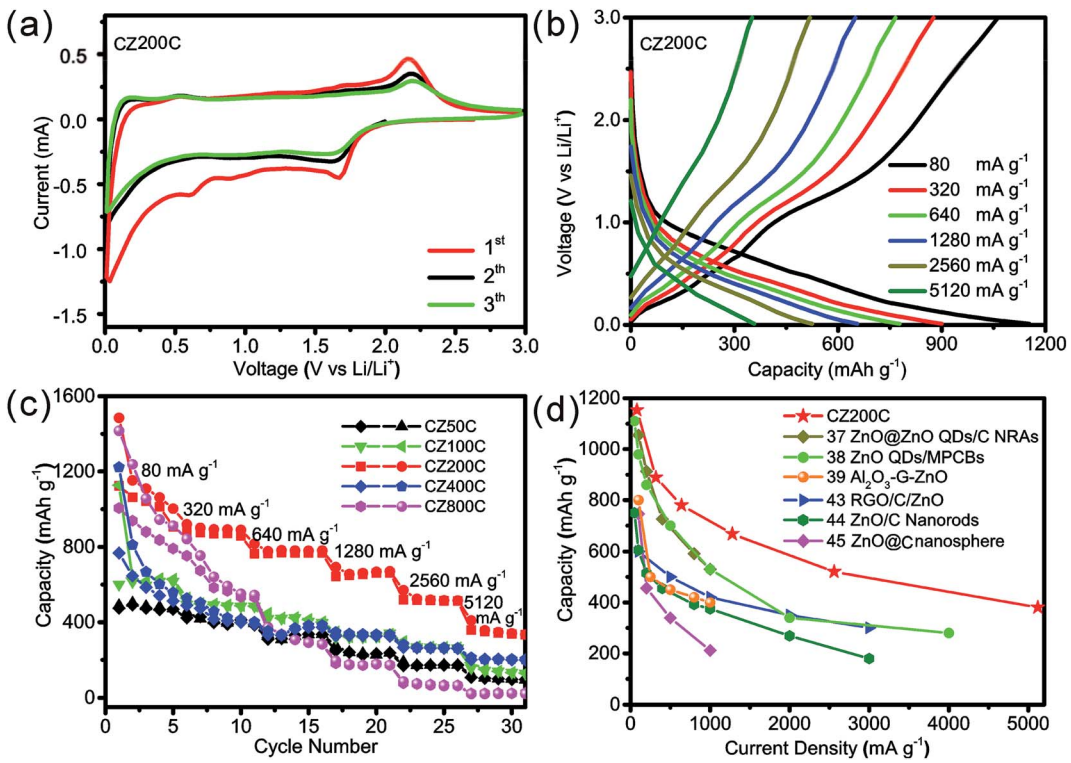

Fig. 2 (a) CV curves of the CZ200C nanosheet anode. (b) Galvanostatic discharge/charge profiles of the CZ200C nanosheet anode. (c) Galvanostatic discharge/charge capacities of CZC nanosheets with 50, 100, 200, 400, and 800 ALD cycles at different current densities. (d) Comparison of the capacity of the CZ200C nanosheet anode with those of ZnO-based anodes reported in recent publications.

a plateau from 1.3 to 2.1 V is observed in the charge profiles (Fig. 2b and S8†) and is ascribed to the oxidation of ZnO, corresponding to the peaks at 1.7 and 2.2 V in the CV anodic scan. The CV results are consistent with the charge/discharge profiles.

The rate performance of the CZC nanosheets was investigated (Fig. 2c). In order to get composite nanosheets with preferable energy density and mechanical stability, composite nanosheets with different ZnO thicknesses (*i.e.*, different numbers of ALD cycles: 50, 100, 200, 400, and 800 cycles in the present work (Fig. S9†)) were tested. For the composite with 50 ALD cycles (CZ50C nanosheets), a steady capacity of 486, 418, 328, 242, 235, and 176 mA h g^{-1} (based on the total mass of the composite) is observed at current densities of 80, 320, 640, 1280, 2560 and 5120 mA g^{-1}, respectively (Fig. 2c). The capacity increases gradually with the number of ALD cycles in the case of a thin ZnO layer because of the higher content of ZnO (Fig. S7†). The CZ200C nanosheet anode demonstrates the highest reversible capacity of 1081 (80 mA g^{-1}), 889 (320 mA g^{-1}), 780 (640 mA g^{-1}), 668 (1280 mA g^{-1}), 520 (2560 mA g^{-1}), and 380 (5120 mA g^{-1}) mA g^{-1} in all 5 samples (as shown in Fig. 2b and c), and the values are also higher than those of previously reported Zn-based anodes (Fig. 2d).[37–39,43–45] However, with further increase of ALD cycles, the CZ400C and CZ800C nanosheet anodes suffer from severe capacity decay (Fig. 2c). With the current increasing from 80 to 640 mA g^{-1}, the CZ400C and CZ800C nanosheets lose 60% and 70% of their initial capacity, respectively. And only around 5% remains with the current density increasing by 64 times for CZ800C nanosheets. When further cycled at 1280 mA g^{-1} for 300 cycles, as shown in Fig. 3a, the CZ200C nanosheet anode retains a capacity of 598 mA h g^{-1}, which is higher than those of CZ100C (470 mA h g^{-1}), CZ400C (405 mA h g^{-1}), CZ50C (300 mA h g^{-1}), and CZ800C (180 mA h g^{-1}). The performance of the batteries was also investigated at even higher current densities. For the CZ100C nanosheet anode, the battery is cycled for 500 cycles at 1250 mA g^{-1}, 500 cycles at 2560 mA g^{-1}, and 1000 cycles at 5120 mA g^{-1}, and no capacity decay occurs (Fig S10†). For the CZ200C nanosheet anode, the battery is cycled at 5000 mA g^{-1} for more than 1450 cycles after cycling for 200 cycles at 4500 mA g^{-1} (Fig. 3b); although a capacity decay of around 8% is observed at the early cycles, it gradually stabilizes at around 330 mA h g^{-1} at a current density of 5000 mA g^{-1}, much higher than that of the CZ100C nanosheet anode. The excellent rate performance of the CZC nanosheet anode with a thinner ZnO layer is ascribed to its unique features. First, in CZC nanosheets, thick carbon coating layers on both sides of the ZnO layer help to provide an electric contact network around ZnO and the porous feature facilitates Li^+ diffusion into the inner ZnO layer.[11,13,27] Second, the thin ZnO nanomembrane inside provides a shortened ion-diffusion length.[3,4] Thus when applied for lithium storage, the composite nanosheets enable fast and high capacity. Besides, because of its flexible properties, the 2D

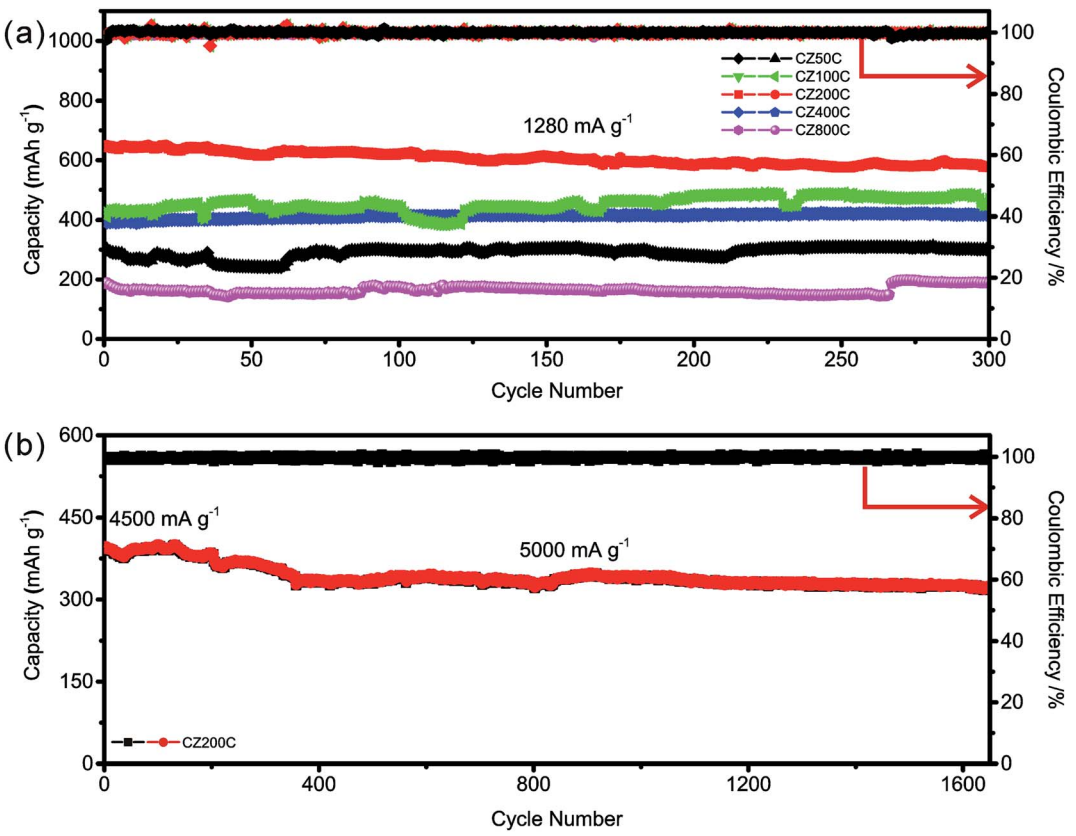

Fig. 3 (a) Cycling performance of the CZC nanosheet anode with 50, 100, 200, 400 and 800 ALD cycles at 1280 mA g^{-1}. (b) Cycling performance of the CZ200C nanosheet anode at 4500 mA g^{-1} for 200 cycles and 5000 mA g^{-1} for 1450 cycles.

nanostructure allows strain accommodation upon lithiation and the carbon coating on the outer layer also helps to restrict the volume change of ZnO.[5,22]

To probe the effect of structural features on the remarkable performance enhancement, we conducted EIS measurements for CZC nanosheet anodes. The Nyquist plots of all samples were recorded and are shown in Fig. 4a and S11.† All the plots for the fresh cell demonstrate a similar shape with one semicircle at high-to-medium frequency (two semicircles for the electrode after cycling, Fig. S11†), followed by the appearance of a straight line at low frequency. The Nyquist plots were carefully analyzed with an equivalent circuit, as depicted in the upper panel of Fig. 4a.[20,31,46–49] Herein, R_e represents the electrolyte resistance. R_{SEI}/CPE_{SEI} from the first semicircle in the high frequency region is attributed to the resistance and capacitance, respectively, due to the formation of a SEI layer on the electrode

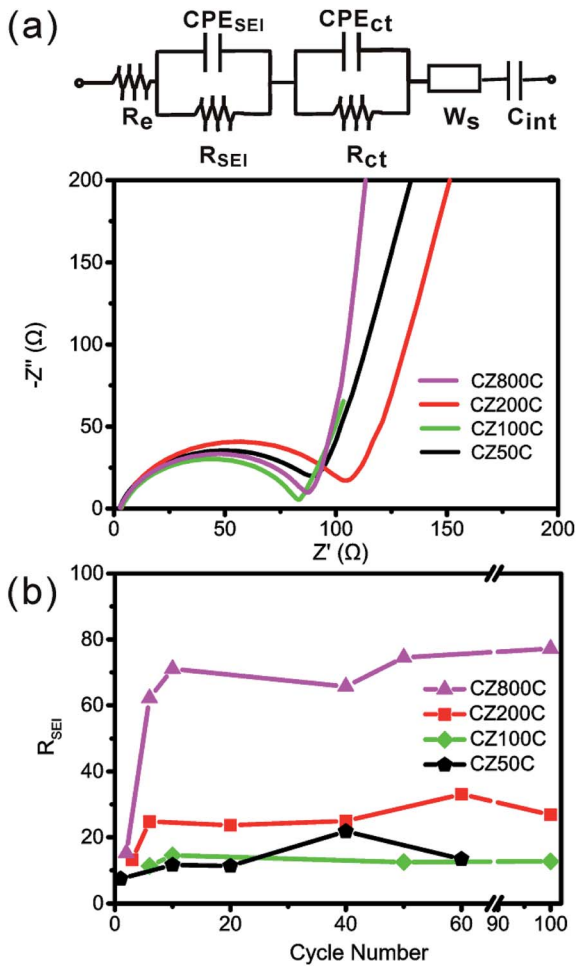

Fig. 4 (a) EIS spectra of CZC nanosheets with 50, 100, 200, and 800 ALD cycles before galvanostatic discharge/charge. The upper panel shows the equivalent circuit used to fit the experimental results. Here R_e, R_{SEI}, and R_{ct} represent the electrolyte resistance (e), SEI resistance, and charge transfer resistance (ct), respectively. CPE is the respective constant-phase element accounting for the depressed semicircle in the experimental spectra. W_s is the Warburg impedance, and C_{int} is the intercalation capacitance. (b) The variation of SEI resistance as a function of the cycle number.

after cycling.[17,27] R_{ct}/CPE_{ct} from the second semicircle is assigned to the charge transfer process. W_s is the Warburg impedance, and C_{int} is the intercalation capacitance, corresponding to the sloping straight line.[47–49] The fresh cells show low resistance, indicating a favorable conducting network and charge transfer at the electrode interface. Fig. 4b lists the values of R_{SEI} after different galvanostatic cycles in the full charge state. For the CZ50C and CZ100C nanosheet anodes, the R_{SEI} remains similar to that of the initial cycle, suggesting a stable SEI. A slightly higher R_{SEI} is observed in the CZ200C nanosheet anode: the R_{SEI} increases to around 25 Ω and becomes stable, while CZ800C exhibits a considerably higher R_{SEI}. The R_{SEI} jumps to around 60 Ω after 5 cycles and finally reaches around 80 Ω (Fig. 4b).

In the present work, we consider that the increase of R_{SEI} is attributed to the growth of the SEI layer, which is caused by cracking of the surface carbon layer. A maximum tensile stress (σ_{max}) will be developed in the carbon layer by the expansion of inner ZnO, and if this stress reaches fracture strength (σ_f), the carbon coating is prone to fracture.[21,22] Previous investigation demonstrated that the tensile stress σ_{max} should increase with the diameter of the oxide core.[22] The stable R_{SEI} of CZ50C and CZ100C nanosheets indicates that tensile stress σ_{max} is less than the fracture strength σ_f, so no crack occurs in the carbon coating. For CZ200C nanosheets, the slightly increased R_{SEI} suggests that σ_{max} is gradually approaching σ_f with increasing ZnO ALD cycles. This consequently leads to a mild crack of the carbon layer and a moderate growth of the SEI layer. The situation is much severer with the further increase of ZnO thickness to 800 ALD cycles because of the much larger tensile stress. In the first several cycles, the SEI layer together with the carbon coating is not robust yet to constrain the lithiation-induced expansion of ZnO. The destruction and regeneration of the SEI layer continues and causes a consecutively increased R_{SEI}.[9] The consumption of electrolyte/Li^+ in the thick SEI and its electrically insulating nature finally induce severe capacity degradation of the CZ800C nanosheet anode.[7–10] Higher ZnO content/larger ZnO thickness (see Fig. S7†) certainly contributes to higher energy density, but a too high ZnO content sacrifices the durability: a high ZnO concentration of 89% in the CZ800C nanosheet anode demonstrates poor stability. Therefore, one may deduce that a critical thickness ratio of the ZnO layer to the carbon layer exists. In the present work, the thicknesses of the carbon layers are constant (Fig. S7†) and the growth rate of ZnO is about 0.16 nm per ALD cycle. Thus, the thickness ratios of ZnO/C are about 1 : 4, 1 : 2, 1 : 1, 2 : 1, and 4 : 1 for CZ50C, CZ100C, CZ200C, CZ400C, and CZ800C, respectively. The mild crack of the carbon layer in CZ200C (Fig. 4b) may suggest that the thickness ratio in CZ200C is close to the critical value. When the thickness ratio of ZnO/C < 1 : 1, as in the cases of CZ50C and CZ100C, a stable cycling performance can be ensured. When the thickness ratio is close to 1 : 1, a slight capacity decay in the early cycles and subsequent stability are noticed. When the thickness ratio > the critical value 1 : 1, as in the cases of CZ400C and CZ800C, the carbon layers are prone to fracture. And an even thicker ZnO layer should lead to severer capacity decay.

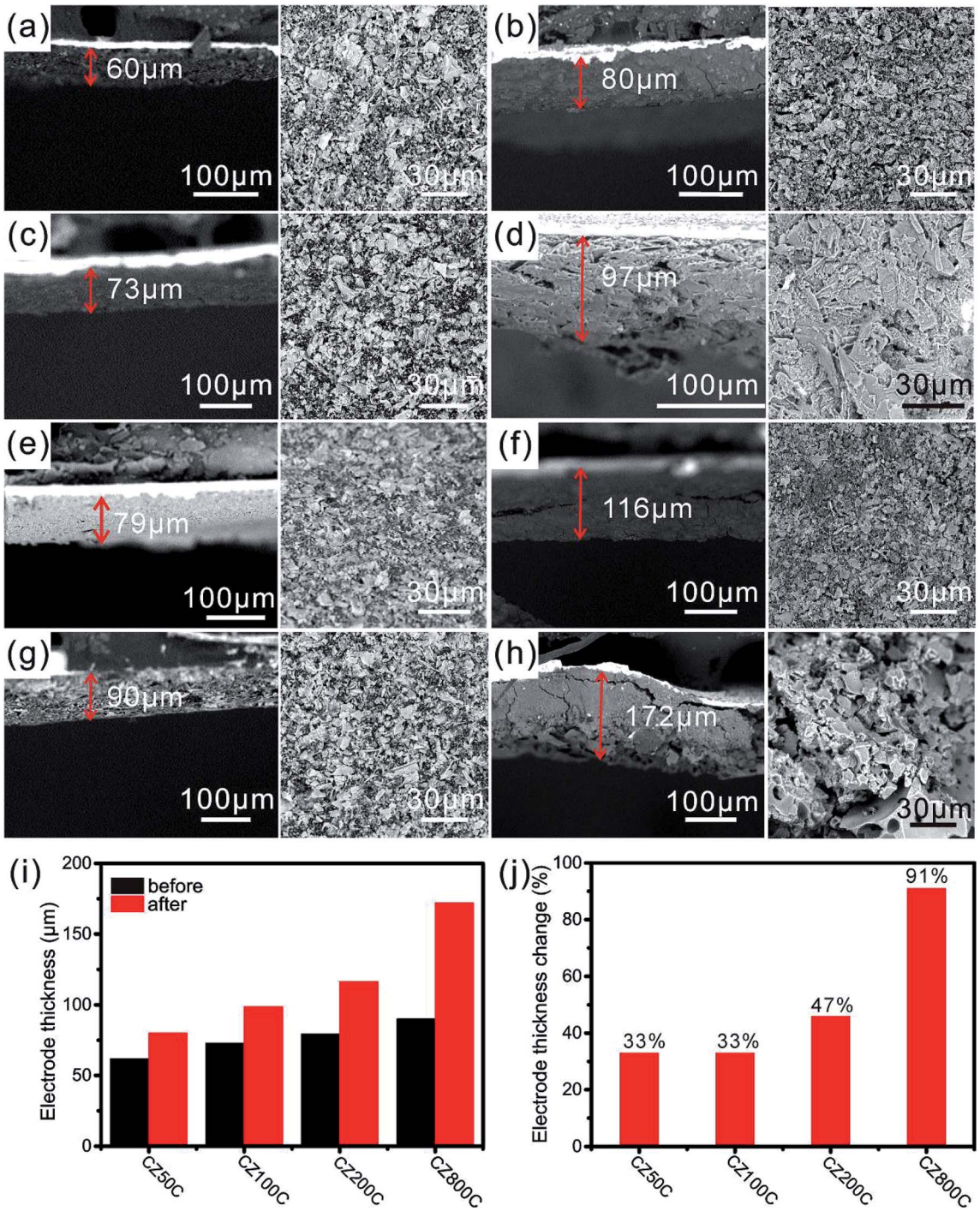

Fig. 5 SEM images demonstrating the change of the electrode structure before and after 200 discharge/charge cycles. (a–h) Cross-sectional view and top view of the CZ50C, CZ100C, CZ200C, and CZ800C electrodes before (a, c, e, and g) and after (b, d, f, and h) 200 cycles. (i) and (j) display the thickness change of all electrodes after 200 discharge/charge cycles.

In order to specifically elucidate the constrain effect of the carbon layer on the ZnO layer in composite CZC nanosheets, we also investigated the volume expansion and structural change of the electrode before and after 200 discharge/charge cycles (Fig. 5). As presented in Fig. 5a and b, for instance, the thickness of the CZ50C nanosheet electrode increases from 60 to 80 μm, with 33% thickness change after 200 cycles. The thickness change of CZ100C nanosheets is 33% and increases to 47% for CZ200C (see also Fig. 5i and j). No significant morphology change can be observed for the electrodes made from CZ50C, CZ100C, and CZ200C nanosheets before and after all charge/discharge cycles, and the nanosheet structure is still distinguishable (Fig. 5b, d, and f). This indicates that when the thickness ratio of ZnO/C $\leq$ 1 : 1, the carbon coating outside

effectively confines the expansion of the ZnO nanosheets and maintains their structural continuity without fracture. However, for the CZ800C nanosheet anode, the electrode exhibits a subversive deformation of surface morphology (Fig. 5g and h). The nanosheets suffer from pulverization due to cracking of the carbon layer and no apparent nanosheets are observed (Fig. 5h). The thickness change reaches 91% (Fig. 5i and j). The comparison of the electrode thickness before and after discharge/charge cycles in Fig. 5i and j implies that, for a thickness ratio of the ZnO layer to the carbon layer below the critical value (~1 : 1), the carbon coating layer in composite nanosheets can sufficiently suppress electrode volume expansion and retain structural integrity after long-term cycling, thereby improving the battery performance compared to the anode with a thicker ZnO layer (*e.g.*, CZ800C nanosheet anode).

Conclusion

Herein, we have designed a sandwiched CZC nanosheet anode with a stable SEI for fast and stable lithium storage. By this means, both CZC and CTC nanosheets (Fig. S12†) were fabricated. The oxide layer with controllable thickness is confined between two porous carbon layers with a thickness larger than 30 nm. In addition to providing an electric contact network around oxides, the thick carbon coating layer helps to suppress the volume change because of its mechanical robustness and facilitates Li^+ transport into the inner ZnO layer due to its porous feature. When used as anodes for lithium storage, the composite nanosheets enable a fast, high and stable capacity. A critical thickness ratio of the ZnO layer to the carbon layer is proposed. If the ZnO layer is thicker, the carbon layer is prone to fracture. This finding provides a guideline for designing sandwiched carbon/oxide/carbon nanostructures for their application in high energy and stable lithium storage.

Conflicts of interest

There are no conflicts to declare.

Acknowledgements

This work is supported by the National Key R&D Program of China (No. 2017YFE0112000), the National Natural Science Foundation of China (No. 61628401 and U1632115), the Science and Technology Commission of Shanghai Municipality (No. 17JC1401700), and the Changjiang Young Scholars Program of China. Part of the work is also supported by the National Key Technologies R&D Program of China (No. 2015ZX02102-003).

Notes and references

1 S. H. Yu, S. H. Lee, D. J. Lee, Y. E. Sung and T. Hyeon, *Small*, 2016, **12**, 2146–2172.
2 M. V. Reddy, G. V. S. Rao and B. V. R. Chowdari, *Chem. Rev.*, 2013, **113**, 5364–5457.
3 J. H. Liu and X. W. Liu, *Adv. Mater.*, 2012, **24**, 4097–4111.
4 J. Mei, T. Liao, L. Z. Kou and Z. Q. Sun, *Adv. Mater.*, 2017, **29**, 1700176.
5 W. P. Si, I. Mönch, C. L. Yan, J. W. Deng, S. L. Li, G. G. Lin, L. Y. Han, Y. F. Mei and O. G. Schmidt, *Adv. Mater.*, 2014, **26**, 7973–7978.
6 S. L. Zhang, K. J. Zhao, T. Zhu and J. Li, *Prog. Mater. Sci.*, 2017, **89**, 491–521.
7 N. Liu, Z. D. Lu, J. Zhao, M. T. Mecdowell, H. W. Lee, W. T. Zhao and Y. Cui, *Nat. Nanotechnol.*, 2014, **9**, 187–192.
8 A. Kushima, X. H. Liu, G. Zhu, Z. L. Wang, J. Y. Huang and J. Li, *Nano Lett.*, 2011, **11**, 4535–4541.
9 H. Wu, G. Chan, J. W. Choi, I. Ryu, Y. Yao, M. T. McDowell, S. W. Lee, A. Jackson, Y. Yang, L. B. Hu and Y. Cui, *Nat. Nanotechnol.*, 2012, **7**, 310–315.
10 D. N. Wang, J. L. Yang, X. F. Li, D. S. Geng, R. Y. Li, M. Cai, T. Sham and X. L. Sun, *Energy Environ. Sci.*, 2013, **6**, 2900–2906.
11 J. B. Wang, Z. W. Liu, W. J. Yang, L. J. Han and M. D. Wei, *Chem. Commun.*, 2018, **54**, 7346–7349.
12 Q. S. Xie, P. F. Liu, D. Q. Zeng, W. J. Xu, L. S. Wang, Z. Z. Zhu, L. M. Mai and D. L. Peng, *Adv. Funct. Mater.*, 2018, **28**, 1707433.
13 W. F. Zhang, T. Xu, Z. W. Liu, N. L. Wu and M. D. Wei, *Chem. Commun.*, 2018, **54**, 1413–1416.
14 W. X. Song, R. Brugge, I. G. Theodorou, A. L. Lim, Y. C. Yang, T. T. Zhao, C. H. Burgess, I. D. Johnson, A. Aguadero, P. R. Shearing, D. J. L. Brett, F. Xie and D. J. Riley, *ACS Appl. Mater. Interfaces*, 2017, **9**, 37823–37831.
15 C. Zheng, M. Y. Liu, W. Q. Chen, L. X. Zeng and M. D. Wei, *J. Mater. Chem. A*, 2016, **4**, 13646–13651.
16 J. Qin, N. Q. Zhao, G. S. Shi, E. Z. Liu, F. He, L. Y. Ma, Q. Y. Li, J. I. Li and C. N. He, *J. Mater. Chem. A*, 2017, **5**, 10946–10956.
17 Y. Zhao, L. P. Wang, S. B. Xi, Y. H. Du, Q. Q. Yao, L. H. Guan and Z. J. Xu, *J. Mater. Chem. A*, 2017, **5**, 25609–25617.
18 J. Liu, M. Z. Gu, L. Z. Ouyang, H. Wang, L. C. Yang and M. Zhu, *ACS Appl. Mater. Interfaces*, 2016, **8**, 8502–8510.
19 W. Q. Yao, J. Chen, L. Zhan, Y. L. Wang and S. B. Yang, *ACS Appl. Mater. Interfaces*, 2017, **9**, 39371–39379.
20 Y. Z. Su, S. Li, D. Q. Wu, F. Zhang, H. W. Liang, P. F. Gao, C. Cheng and X. L. Feng, *ACS Nano*, 2012, **6**, 8349–8356.
21 W. Q. Li, K. Cao, H. T. Wang, J. B. Liu, L. M. Zhou and H. M. Yao, *Nanoscale*, 2016, **8**, 5254–5259.
22 Q. Q. Li, W. Q. Li, Q. Feng, P. Wang, M. M. Mao, J. B. Liu, L. M. Zhou, H. T. Wang and H. M. Yao, *Carbon*, 2014, **80**, 793–798.
23 B. Luo, B. Wang, X. L. Li, Y. Y. Jia, M. H. Liang and L. J. Zhi, *Adv. Mater.*, 2012, **24**, 3538–3543.
24 W. Q. Li, Q. Wang, K. Cao, J. J. Tang, H. T. Wang, L. M. Zhou and H. M. Yao, *Compos. Commun.*, 2016, **1**, 1–5.
25 J. Y. Cheong, J. H. Chang and C. Kim, *Electrochim. Acta*, 2017, **258**, 1140–1148.
26 L. L. Peng, Z. W. Fang, Y. Zhu, C. S. Yan and G. H. Yu, *Adv. Energy Mater.*, 2018, **8**, 1702179.
27 L. L. Peng, P. Xiong, L. Ma, Y. F. Yuan, Y. Zhu, D. H. Chen, X. Y. Luo, J. Lu, K. Amine and G. H. Yu, *Nat. Commun.*, 2017, **8**, 15139.

28 Y. B. Liu, M. H. Guo, Z. W. Liu, Q. H. Wei and M. D. Wei, *J. Mater. Chem. A*, 2018, **6**, 1196–1200.
29 H. Q. Li and H. S. Zhou, *Chem. Commun.*, 2012, **48**, 1202–1217.
30 D. M. Yang, Q. Lu, Z. Y. Fan, S. M. Li, J. J. Tu and W. Wang, *J. Appl. Polym. Sci.*, 2010, **118**, 2304–2313.
31 Y. T. Zhao, G. S. Huang, Y. L. Li, R. Edy, P. B. Gao, Z. H. Bao and Y. F. Mei, *J. Mater. Chem. A*, 2018, **6**, 7227–7235.
32 S. Q. Pan, Y. T. Zhao, G. S. Huang, J. Wang, S. Baunack, T. Gemming, M. L. Li, L. R. Li, O. G. Schmidt and Y. F. Mei, *Nanotechnology*, 2015, **26**, 364001.
33 V. Etacheri, C. N. Hong and V. G. Pol, *Environ. Sci. Technol.*, 2015, **49**, 11191–11198.
34 L. Yao, Q. Wu, P. X. Zhang, J. M. Zhang, D. R. Wang, Y. L. Li, X. Z. Ren, H. W. Mi, L. B. Deng and Z. J. Zheng, *Adv. Mater.*, 2018, **30**, 1706054.
35 R. Font, A. Fullana, J. A. Caballero, J. Candela and A. Garcıa, *J. Anal. Appl. Pyrolysis*, 2001, **58–59**, 63–77.
36 A. Bazargan and G. Mckay, *Chem. Eng. J.*, 2013, **195–196**, 377.
37 G. H. Zhang, S. C. Hou, H. Zhang, W. Zeng, F. L. Yan, C. C. Li and H. G. Duan, *Adv. Mater.*, 2015, **27**, 2400–2405.
38 Z. M. Tu, G. Z. Yang, H. W. Song and C. X. Wang, *ACS Appl. Mater. Interfaces*, 2017, **9**, 439–446.
39 M. P. Yu, A. J. Wang, C. Li and G. Q. Shi, *Nanoscale*, 2014, **6**, 11419–11424.
40 X. H. Huang, X. H. Xia, Y. F. Yuan and F. Zhou, *Electrochim. Acta*, 2011, **56**, 4960–4965.
41 H. C. Liu, L. D. Shi, D. Z. Li, J. L. Yu, H. M. Zhang, S. H. Ullah, B. Yang, C. H. Li, C. Z. Zhu and J. Xu, *J. Power Sources*, 2018, **387**, 64–71.
42 Q. S. Xie, P. F. Liu, D. Q. Zeng, W. J. Xu, L. S. Wang, Z. Z. Zhu, L. Q. Mai and D. L. Peng, *Adv. Funct. Mater.*, 2018, **28**, 1707433.
43 S. Wi, H. Woo, S. Lee, J. Kang, J. Kim, S. An, C. Kim, S. Nam, C. Kim and B. Park, *Nanoscale Res. Lett.*, 2015, **10**, 204.
44 J. P. Liu, Y. Y. Li, R. M. Ding, J. Jiang, Y. Y. Hu, X. X. Ji, Q. B. Chi, Z. H. Zhu and X. T. Huang, *J. Phys. Chem. C*, 2009, **113**, 5336–5339.
45 Y. Liu, Y. Li, M. Zhong, Y. M. Hu, P. F. Hu, M. Y. Zhu, W. X. Li and Y. B. Li, *Mater. Lett.*, 2016, **171**, 244–247.
46 Y. L. Li, Y. T. Zhao, G. S. Huang, B. R. Xu, B. Wang, R. B. Pan, C. L. Men and Y. F. Mei, *ACS Appl. Mater. Interfaces*, 2017, **9**, 38522–38529.
47 H. L. Pan, J. Z. Chen, R. G. Cao, V. J. Murugesan, N. N. Rajput, K. S. Han, K. Persson, L. Estevez, M. H. Engelhard, J. G. Zhang, K. T. Mueller, Y. Cui, Y. Y. Shao and J. Liu, *Nat. Energy*, 2017, **2**, 813–820.
48 N. Ogihara, Y. Itou, T. Sasaki and Y. Takeuchi, *J. Phys. Chem. C*, 2015, **119**, 4612–4619.
49 S. S. Zhang, K. Xu and T. R. Jow, *Electrochim. Acta*, 2006, **51**, 1636–1640.